Chinese Chemical Letters 33 (2022) 462–465

Contents lists available at ScienceDirect

Chinese Chemical Letters

journal homepage: www.elsevier.com/locate/cclet

Three-dimensional $Co_2V_2O_7 \cdot nH_2O$ superstructures assembled by nanosheets for electrochemical energy storage

Nan Li, Xiaowen Guo, Xinru Tang, Yichen Xing, Huan Pang*

School of Chemistry and Chemical Engineering, Yangzhou University, Yangzhou 225009, China

ARTICLE INFO

Article history:
Received 7 April 2021
Revised 3 May 2021
Accepted 10 May 2021
Available online 19 May 2021

Keywords:
Superstructure
Hydrothermal method
High stability
$Co_2V_2O_7 \cdot nH_2O$
Energy storage

ABSTRACT

Hierarchical superstructures assembled by nanosheets can effectively prevent aggregation of nanosheets and improve performance in energy storage. Therefore, we proposed a facile hydrothermal method to obtain three-dimensional (3D) superstructure assembled by nanosheets. We found that the ratio of Co^{2+}/HMTA affected the morphology of the samples, and the 3D hierarchical structures of are obtained while the ratio of Co^{2+}/HMTA is 12:25. The hierarchical structures with sufficient interior space preserves the original sheet-like dimensional components and results in sufficient active sites and efficient mass diffusion. Hence, the 3D $Co_2V_2O_7 \cdot nH_2O$ hierarchical structure exhibits good rate capability and high stability while as electrode materials. Meanwhile, when power density is 745.13 W/kg, the assembled CVO-2//AC shows an energy density of 47.7 Wh/kg. The work displays a facile method for fabrication of 3D superstructure assembled by 2D nanosheets that can be applied in energy storage.

© 2021 Published by Elsevier B.V. on behalf of Chinese Chemical Society and Institute of Materia Medica, Chinese Academy of Medical Sciences.

As we known, the materials composition and structures, involving crystal orientations, configurations and particle sizes have an eventful role in the performance. Morphology engineering is a valid way to improve the electrochemical performance [1–10]. Low-dimensional materials (nanoparticles, nanorods, nanosheets or nanoplates) are potential materials due to their high surface-to-volume ratios, high exposed facets, and excellent charge-transport abilities. However, their applications were limited because the material is prone to agglomeration. So designing assemblies constructed with low dimensional materials is a promising approach. It is clear that three-dimensional (3D) architectures composed of different building units have exhibited excellent performance in energy storage [11–17]. 3D materials composed of low dimensional nanostructure can promote structure stability and resistance to aggregation, which not only facilitates sufficient contact with electrolyte, but also ensures fast intercalation of ions and rapid charge transfer, which results in enhanced electrochemical performance [18–21]. For example, Xu *et al.* [22] reported a novel porous 3D superstructures of carbon nanosheets decorated with ultrafine cobalt phosphide nanoparticles for electrocatalysis. The structure ensures abundant surface catalytic sites and promote better mass and electrons mobility. Wang *et al.* [20] reported a novel hierarchical Co(OH)F superstructures for efficient oxygen evolution reaction electrocatalysis. The structure ensures abundant surface catalytic sites and promote better charge mobility. Yan *et al.* [23] successfully obtained a novel accordion-like Ni-MOF superstructure, which as electrode material showed a high specific capacitances of 988 F/g at 1.4 A/g and outstanding cycling stability of 96.5% after 5000 cycles. However, the fabrication of 3D superstructures composed of low dimensional nanostructure is still a challenge [24–26].

The demand for economical and energy storage technology has promoted the development of energy storage. Supercapacitors (SCs) are attractive due to fast charging/discharging rate, low cost, excellent power density and good cycling stability [2,27–32]. To meet the growing demand for SCs with performances, transition metal oxides (TMOs) as a class of pseudocapacitive materials have caught great attention in virtue of their high theoretical specific capacity, widespread availability, reinforced safety and low cost. The redox-active TMOs exhibit higher pseudocapacitance than conventional carbon materials, making them desirable candidates as the next generation-electrochemical energy storage devices [33–39]. Among numerous electrode materials, vanadium oxides have been widely studied as potential alternatives for SCs because of the various structures of compound and multiple valence state of vanadium [40–42]. Hence, the equitable design of TMOs architecture by a facile method is essential for achieving high performance.

In this work, we construct successfully uniform $Co_2V_2O_7 \cdot nH_2O$ superstructure assembled by nanosheets using a hydrothermal method at 80 °C. By adjusting the amount of Co^{2+}/HMTA involved in the reaction, uniform $Co_2V_2O_7 \cdot nH_2O$ superstructure could be

* Corresponding author.
E-mail address: panghuan@yzu.edu.cn (H. Pang).

https://doi.org/10.1016/j.cclet.2021.05.012
1001-8417/© 2021 Published by Elsevier B.V. on behalf of Chinese Chemical Society and Institute of Materia Medica, Chinese Academy of Medical Sciences.

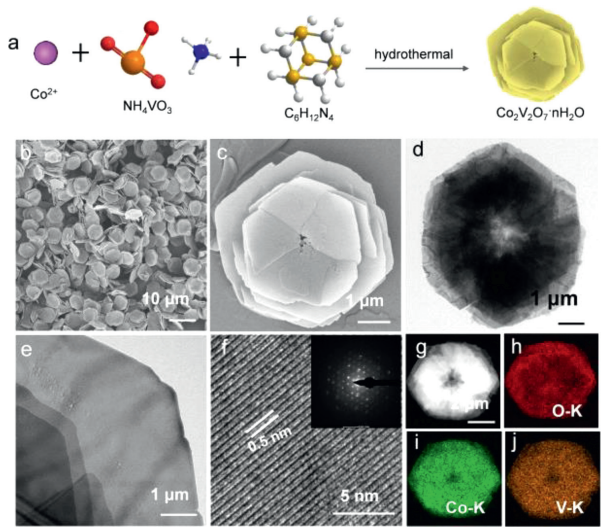

Fig. 1. (a) Schematic diagram of the synthesis of the 3D CVO-2. (b,c) SEM images of CVO-2. (d,e) TEM images of CVO-2. (f) HRTEM images of CVO-2 (inset of (f): SAED pattern). (g–j) EDS-mapping images of (h) O, (i) Co, (j) V.

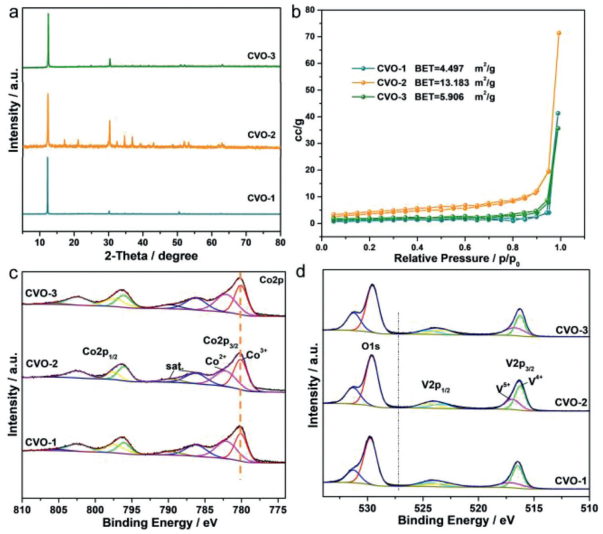

Fig. 2. (a) XRD pattern of CVO-1, CVO-2 and CVO-3. (b) N_2 adsorption-desorption isotherms of CVO-1, CVO-2 and CVO-3. (c) Co 2p spectra of the CVO-1, CVO-2 and CVO-3. (d) O 1s and V 2p spectra of the CVO-1, CVO-2 and CVO-3.

obtained. It is found that the molar ratio of Co^{2+}/HMTA is crucial to the preparation of 3D $Co_2V_2O_7{\cdot}nH_2O$ superstructure. The structure ensures large ion contact surface and increases electroactive sites. Subsequently, we studied the electrochemical performance of the prepared $Co_2V_2O_7{\cdot}nH_2O$ by three-electrode system. $Co_2V_2O_7{\cdot}nH_2O$ hierarchical structure electrode illustrates a specific capacity of 302.1 F/g at 1 A/g. And specific capacity maintains at 92.83% after 4000 cycles at 5 A/g. Moreover, aqueous devices are assembled, and the maximum specific capacitance of $Co_2V_2O_7{\cdot}nH_2O$ hierarchical structure is 153.41 F/g. which could be a potential material for SCs with a superior performance.

As shown in Fig. 1a, products were synthesized by the hydrothermal method. First, $CoCl_2{\cdot}6H_2O$ and NH_4VO_3 were mixed at 80 °C. Then HMTA was added into the above solution. Finally, the resulting solution was reacted 4 h at 80 °C. Interestingly, the HMTA is as a pH regulator, and the different molar ratios of Co^{2+} and HMTA affect the morphology of samples. During the process, the possible reactions can be as follows:

$$C_6N_4H_{12} + 6H_2O \leftrightarrow 4NH_3 + 6HCHO \quad (1)$$

$$NH_3 + H_2O \leftrightarrow NH_4^+ + OH^- \quad (2)$$

$$2Co^{2+} + 2VO^{3-} + 2OH^- + (n\text{-}1)H_2O \leftrightarrow Co_2V_2O_7{\cdot}nH_2O \quad (3)$$

The morphology of the prepared materials is examined by scanning electron microscopy (SEM). As shown in Figs. 1b and c and Fig. S1 (Supporting information) (Co^{2+}:HMTA = 2:25, 6:25, 8:25, 10:25, 12:25 and 14:25), when the ratio of Co^{2+}:HMTA is relatively low, the he samples are monodisperse hexagonal platelets (CVO-1, Co^{2+}:HMTA = 2:25). With the increasing ratio of Co^{2+}:HMTA, the morphology of the hexagonal platelets gradually transformed into 3D $Co_2V_2O_7{\cdot}nH_2O$ hierarchical structure (CVO-2, Co^{2+}:HMTA = 12:25). As the ratio of Co^{2+}/HMT is increased to 14:25, uneven sheets were obtained (CVO-3). Comparing above results found the higher ratio of Co^{2+}/HMTA is favorable for the preparation of sheet-like structures.

CVO-2 is chosen to research the detailed structure of the end-product. CVO-2 is further assessed by using transmission electron microscopy (TEM). The low-magnification TEM images are shown in Figs. 1d and e, which illustrates that the CVO-2 has the hierarchical structure assembled by ultrathin sheets. The high-resolution TEM (HRTEM) image (Fig. 1f) shows lattice fringe with a spacing of 0.5 nm corresponds to the d-spacing of (100) planes of $Co_2V_2O_7{\cdot}nH_2O$ [43]. In the selected area electron diffraction (SAED) (inset of Fig. 1f) finds a mass of points arranged regularly, suggesting CVO-2 is the single crystal structure. Furthermore, CVO-2 comprises Co, V and O, as affirmed by energy-dispersive X-ray spectroscopy mapping (EDS mapping) (Figs. 1g–j), and Co, V and O are evenly dispersed throughout the CVO-2. Notably, under the same ratio of Co^{2+}/HMTA, when other temperature conditions were substituted, we cannot synthesize a sample consisting of uniform layered structure (Fig. S2 in Supporting information). Moreover, we tried to confirm the effect of HMTA on the morphology. When the reaction time was 4 h, the HMTA was altered to 1 mmol, 2 mmol and 10 mmol, and the other conditions were equivalent. The relevant SEM images are displayed in Fig. S3 (Supporting information). It could be found from SEM images that of the 5 mmol is optimum for the synthesis of $Co_2V_2O_7{\cdot}nH_2O$ hierarchical structure.

X-ray diffraction (XRD) of the as-obtained $Co_2V_2O_7{\cdot}nH_2O$ are displayed in Fig. 2a. The XRD result of $Co_2V_2O_7{\cdot}nH_2O$ can match with reported in the literature [43]. The strong diffraction peaks show the good crystallinity of the as-obtained product. As shown in Fig. S4 (Supporting information), the thermal behavior of the CVO-2 sample is tested by thermogravimetric analysis (TGA). The weight loss of the CVO-2 sample is 13.2%, implying that n is near 2.8, which confirms that CVO-2 sample is $Co_2V_2O_7{\cdot}2.8H_2O$.

Fig. S5 (Supporting information) displays the Fourier transform infrared spectrometer (FTIR) of the as-prepared products. The symmetric and asymmetric stretching vibration peaks of the V-O band and the stretching vibration mode of the V=O band are in the range from 400 cm^{-1} to 1000 cm^{-1}. The relatively weak peak at about 480 cm^{-1} can be assigned to the stretching of Co-O modes. The peaks at 1611 and 3514 cm^{-1} are corresponded to the bending vibration and symmetric stretching vibration of H-O-H in H_2O, respectively. The peak at 3114 cm^{-1} can be characteristics of the OH^-.

The X-ray photoelectron spectroscopy (XPS) results also confirm the successful fabrication of CVO-1, CVO-2 and CVO-3. As displayed in Fig. S6 (Supporting information), the XPS survey spectra illustrate that Co, V and O could be observed. The two distinct Co $2p_{3/2}$ peaks locate at 780.12 and 782.29 eV in the Co 2p spectra of Fig. 2c, which are ascribed to Co^{3+} and Co^{2+}, respectively. The

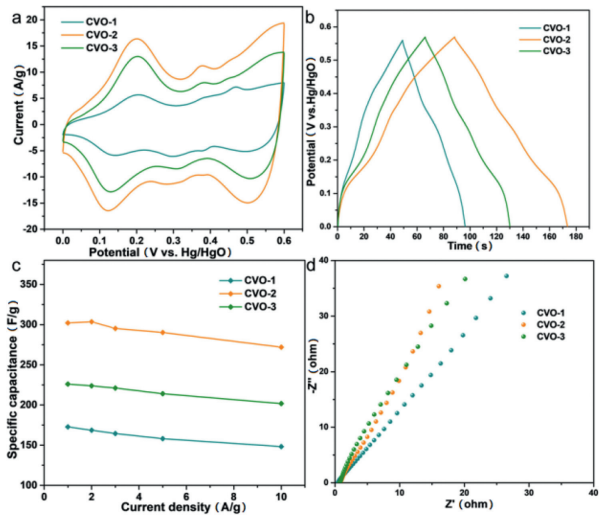

Fig. 3. Electrochemical data of as-obtained CVO-1, CVO-2 and CVO-3 in three-electrode system. (a) The CV curves at 50 mV/s. (b) The GCD curves at 2 A/g. (c) Specific capacitances at various current densities. (d) The EIS plot.

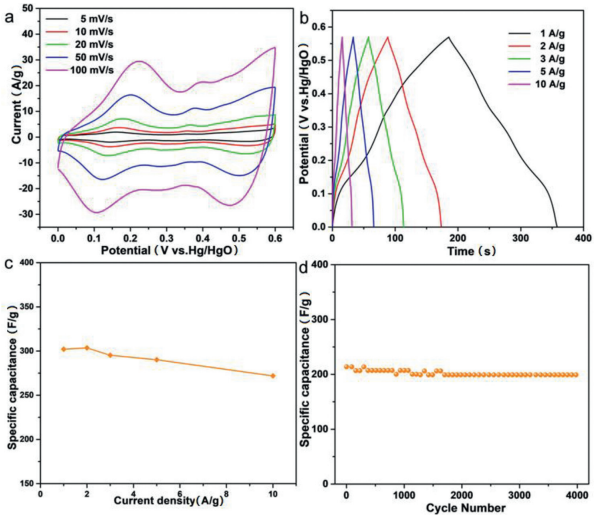

Fig. 4. Electrochemical data of as-obtained CVO-2 in three electrode system. (a) The CV curves at different scan rates. (b) The GCD at different current densities. (c) Specific capacitances at various current densities. (d) Charge/discharge cycling at a current density of 5 A/g.

binding energies of Co in the three samples are not shifted. The V 2p spectra of CVO-1, CVO-2 and CVO-3 (Fig. 2d) demonstrate that the binding energies for V $2p_{3/2}$ at 516.21 eV and 517.01 eV belong to the V^{4+} and V^{5+}, respectively. The O 1s spectra of CVO-1, CVO-2 and CVO-3 (Fig. 2d) can be fitted by two peaks at 531.3 and 529.6 eV. The peak at 529.6 eV refers to the characteristics of O in the metal oxide, and the other peak at around 531.3 eV indicates the existence of OH^- or adsorbed H_2O.

In addition, the CVO-2 samples exhibit Brunauer-Emmett-Teller (BET) surface area of 13.183 m^2/g, whereas the other two samples show the BET surface areas of 4.497 m^2/g (CVO-1) and 5.506 m^2/g (CVO-3), respectively (Fig. 2b). The hierarchical structure confirms the as-obtained materials with much easier contact with the electrolyte, which may increase active sites for redox reactions and shorten ion diffusion lengths.

The as-obtained $Co_2V_2O_7{\cdot}nH_2O$ samples are tested as SCs electrodes in three-electrode system and the results are showed in Fig. 3. Their cyclic voltammogram (CV) curves (Fig. 3a) show that the surrounding area of CVO-2 is larger than that of other $Co_2V_2O_7{\cdot}nH_2O$ materials. It is obviously that the redox peaks are due to the reversible redox reaction. Fig. 3b is the galvanostatic charge-discharge (GCD) curves of the $Co_2V_2O_7{\cdot}nH_2O$, which suggest that charge-discharge time of CVO-2 is the longest at 2 A/g, implying that the capability of CVO-2 is much better than that of the other two materials. The possible reason is that the layered structure is more conducive to sufficient contact with the electrolyte and facilitates the rapid ion transport. The charge-storage mechanism of $Co_2V_2O_7{\cdot}nH_2O$ probably can be described as following:

$$Co^{2+} + 2OH^- \leftrightarrow Co(OH)_2 \quad (4)$$

$$Co(OH)_2 + OH^- \leftrightarrow CoOOH + H_2O + e^- \quad (5)$$

$$CoOOH + OH^- \leftrightarrow CoO_2 + H_2O + e^- \quad (6)$$

As displayed in Fig. 3c, the specific capacitance is obtained in range of 1 A/g to 10 A/g. It is apparent that the specific capacity of CVO-2 hierarchical structure is much higher than that of hexagonal CVO-1 and uneven sheets CVO-3 in that range, which can be attributed to the fact: CVO-2 hierarchical structure assembled by 2D nanosheets ensures large ion contact surface and increased electroactive sites. Especially, the CVO-2 electrode exhibits a specific capacity of 302.1 F/g at 1 A/g. Moreover, the electrode exhibits a specific capacitance of 271.9 F/g at 10 A/g, showing 90% rate capability. Additionally, the electrochemical impedance spectra (EIS) of the electrodes (Fig. 3d) shows that the CVO-2 possesses a smaller charge transfer resistance than that of the other two materials, indicating that the CVO-2 has and better ion transfer capability.

The CV curves of the CVO-2 electrode at various scan rates from 5 mV/s to 100 mV/s are illustrated in Fig. 4a. The shape of CV curves is symmetric at various scan rates within 0–0.6 V. The high symmetry can be due to the reversibility of the faradaic reaction, implying the pseudocapacitive characteristics of CVO-2 electrode. And the shape of CV curves maintains the same, confirming the good reversibility of the $Co_2V_2O_7{\cdot}nH_2O$ electrode. And the higher the scan rate of the CV curves, the larger closed region is acquired, which is due to the high charge mobility at higher scan rate. Additionally, the CV curves of hexagonal CVO-1 and uneven sheets CVO-3 are measured and the results are displayed in Fig. S7 (Supporting information), which shows a similar pattern to the CV curve of CVO-2. Based on Fig. 4a and Fig. S7, the linear plots of the peak currents (I) and $\nu^{1/2}$ (scan rate: ν) are shown in Fig. S8 (Supporting information), indicating that the redox reaction of the electrodes is mainly controlled by the diffusion process. Furthermore, Fig. 4b illustrates the GCD curves of the CVO-2 hierarchical structure electrode at 1–10 A/g. The charging/discharging curves are nearly symmetric, confirming the fast and reversible redox reactions and good coulombic efficiency of the CVO-2 material. The specific capacity is calculated from the GCD curves and the results are shown in Fig. 4c, which are 302.1, 303.6, 295.3, 290.2 and 271.9 F/g, respectively. The GCD curves of CVO-1 and CVO-3 are displayed in Fig. S9 (Supporting information). The cycling performance of the CVO-2 sample is demonstrated in Fig. 4d at 5 A/g. From the cycling performance, it is obvious that the capacitance is retained up to 92.83% after 4000 cycles. The SEM images of CVO-2 after 4000 cycles is shown in Fig. S10 (Supporting information). The result shows that the CVO-2 electrode still maintains a layered structure after 4000 cycles, which indicates that the CVO-2 sample has good structural stability. The Comparison of SCs performance of CVO-2 and other oxide materials reported is shown in Table S1 (Supporting information).

Aqueous devices are constructed with the $Co_2V_2O_7{\cdot}nH_2O$ as a positive material, while activated carbon as a negative material

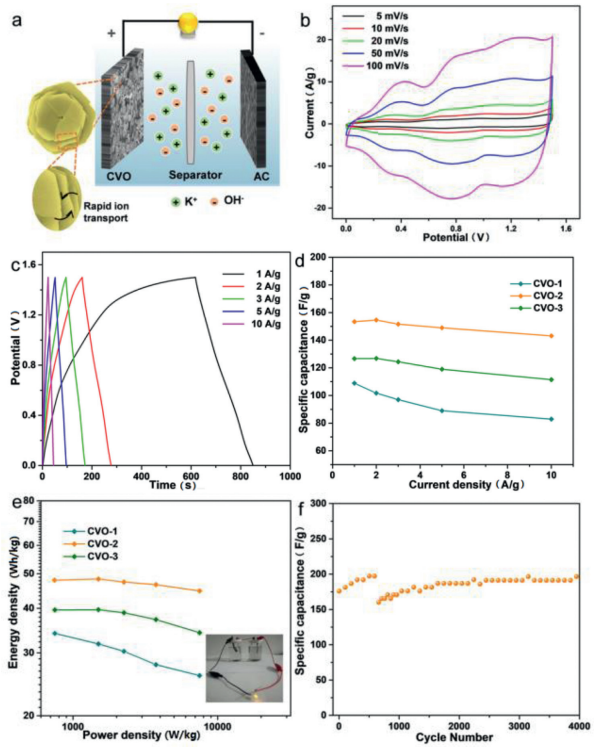

Fig. 5. Electrochemical results of as-prepared $Co_2V_2O_7{\cdot}nH_2O$ in aqueous devices. (a) Schematic diagram of the assembled aqueous devices. (b) The CV curves at different scan rates of CVO-2. (c) The GCD curves at different current densities of CVO-2. (d) Specific capacitances at different current densities of CVO-1, CVO-2 and CVO-3. (e) Ragone plot of the $Co_2V_2O_7{\cdot}nH_2O$//AC aqueous device between energy density and power density (inset: a LED powered by aqueous devices). (f) Cyclic capacitance of CVO-2 at 5 A/g.

(Fig. 5a). As seen in Fig. 5b, CV curves of CVO-2 remain well-shaped in the range of 5–100 mV/s, indicating good rate performance. The GCD curves of CVO-2 at various current densities are shown in Fig. 5c, The and CV and GCD curves of hexagonal CVO-1 and uneven sheets CVO-3 are given in Figs. S11 and S12 (Supporting information). On basis of the GCD curves, the obtained specific capacity of the CVO-2//AC aqueous device are 153.41, 154.6, 151.6, 149 and 143.13 F/g (Fig. 5d), which are superior to other two products. The higher specific capacity of CVO-2 further confirms that they can be potential as an electrode for SCs. The overall performance of as-prepared materials//AC devices can be get from the Ragone plots (Fig. 5e) that displays the relationship between the power density and energy density of the aqueous devices on basis of the GCD curves. The results reveal that rate property of CVO-2//AC is superior to other products, with good energy density of 47.7 Wh/kg at power density of 745.13 W/kg. Additionally, the cyclic stability of CVO-2 is examined (Fig. 5f). The CVO-2//AC presented good cycle stability after 4000 cycles.

In this work, $Co_2V_2O_7{\cdot}nH_2O$ hierarchical structure is rapidly prepared at 80 °C for 4 h by hydrothermal method. The structure and performance of the materials at various ratios of Co^{2+}/HMTA are explored. Impressively, the uniform $Co_2V_2O_7{\cdot}nH_2O$ hierarchical structure piled up orderly at optimum condition. The $Co_2V_2O_7{\cdot}nH_2O$ hierarchical structure as electrodes presents good stability (92.83% retention at 5 A/g after 4000 cycles). The good performance can be ascribed to the fact that the hierarchical structures ensure electrode sufficient contact with electrolyte and sufficient preserves the original sheet-like dimensional components. The nanosheets orderly piled up can provide sufficient spaces, which is conducive to ion transport and results in sufficient active sites. And at a high power density of 745.13 W/kg, the CVO-2//AC displays the electrochemical property with an energy density of 47.7 Wh/kg. Such structure reveals that $Co_2V_2O_7{\cdot}nH_2O$ is prospective material for practical application in SCs.

Declaration of competing interest

The authors declare that they have no known competing financial interests or personal relationships that could have appeared to influence the work reported in this paper.

Acknowledgements

This work was supported by the National Natural Science Foundation of China (Nos. NSFC-U1904215 and 21671170), and the Top-notch Academic Programs Project of Jiangsu Higher Education Institutions (TAPP). Program for Young Changjiang Scholars of the Ministry of Education, China (No. Q2018270). We also acknowledge the Priority Academic Program Development of Jiangsu Higher Education Institutions.

Supplementary materials

Supplementary material associated with this article can be found, in the online version, at doi:10.1016/j.cclet.2021.05.012.

References

[1] D. Zhao, M. Dai, H. Liu, et al., Adv. Mater. Interfaces 6 (2019) 1901308.
[2] C. Qu, Z. Liang, Y. Jiao, et al., Small 14 (2018) 1800285.
[3] L. Jin, H. Pang, Chin. Chem. Lett. 31 (2020) 2300–2304.
[4] J. Chen, L. Zhang, W. Bai, et al., Electrochim. Acta 337 (2020) 135824.
[5] D.P. Wang, M. Fu, Y. Ha, H. Wang, R. Wu, J. Colloid Interface Sci. 529 (2018) 265–272.
[6] J.L. Wang, H.J. Jiang, Z. He, et al., Nano Lett. 20 (2020) 2763–2769.
[7] C.L. Zhang, B.R. Lu, F.H. Cao, et al., J. Mater. Chem. A 6 (2018) 12962–12968.
[8] W. Liu, R. Yin, X. Xu, et al., Adv. Sci. 6 (2019) 1802373.
[9] B. Li, B. Xi, Z. Feng, et al., Adv. Mater. 30 (2018) 1705788.
[10] X. Guo, N. Li, Y. Cheng, et al., Chem. Eng. J. 411 (2021) 128544.
[11] G.Q. Yuan, S.K. Yu, J. Jie, et al., Chin. Chem. Lett. 31 (2020) 1941–1945.
[12] K. Yan, Z. Liang, Z. Li, et al., CrystEngComm 20 (2018) 5249–5255.
[13] Y. Ma, X. Wang, X. Sun, T. Gao, Y. Liu, Inorg. Chem. Front. 5 (2018) 1199–1206.
[14] L. Zou, M. Kitta, J. Hong, et al., Adv. Mater. 1900440 (2019) 1900440.
[15] F.X. Ma, L. Yu, C.Y. Xu, X.W. Lou, Energy Environ. Sci. 9 (2016) 862–866.
[16] W. Liu, L. Yu, R. Yin, et al., Small 16 (2020) 1906775.
[17] X. Xu, W. Shi, W. Liu, et al., J. Mater. Chem. A 6 (2018) 24086–24091.
[18] X. Wu, J. Chen, C. Tan, et al., Nat. Chem. 8 (2016) 470–475.
[19] S.Q. Wu, Z. Hu, Energy Environ. Sci. 9 (2016) 2053–2060.
[20] S. Wan, J. Qi, W. Zhang, et al., Adv. Mater. 29 (2017) 1700286.
[21] M. Chen, Y. Zhang, L. Xing, Y. Liao, Y. Qiu, Adv. Mater. 29 (2017) 1607015.
[22] C.C. Hou, L. Zou, Y. Wang, Q. Xu, Angew. Chem. Int. Ed. 59 (2020) 21360–21366.
[23] Y. Yan, P. Gu, S. Zheng, et al., J. Mater. Chem. A 4 (2016) 19078–19085.
[24] Y. Wang, H. Chai, H. Dong, et al., ACS Appl. Mater. Interfaces 8 (2016) 27291–27297.
[25] M.C. Liu, L. Bin Kong, L. Kang, et al., J. Mater. Chem. A 2 (2014) 4919–4926.
[26] J. Zhang, B. Yuan, S. Cui, et al., Dalton Trans. 46 (2017) 3295–3302.
[27] S. Zheng, X. Li, B. Yan, et al., Adv. Energy Mater. 7 (2017) 1602733.
[28] H.Y. Duan, T. Wang, X.Y. Wu, et al., Chin. Chem. Lett. 31 (2020) 2330–2332.
[29] Y. Zhou, Z. Jia, L. Shi, et al., Chem. Eng. J. 385 (2020) 123858.
[30] Y. Tao, J. Yuan, X. Qian, et al., Inorg. Chem. Front. 8 (2021) 2271–2279.
[31] J.C. Li, J. Gong, X. Zhang, et al., ACS Appl. Energy Mater. 3 (2020) 3692–3703.
[32] Y. Li, Y. Shan, H. Pang, Chin. Chem. Lett. 31 (2020) 2280–2286.
[33] X. Luo, M. Zhong, P. He, et al., J. Alloy. Compd. 826 (2020) 154241.
[34] C. Guan, X. Liu, W. Ren, et al., Adv. Energy Mater. 7 (2017) 1602391.
[35] Y.Z. Zhang, Y. Wang, Y.L. Xie, et al., Nanoscale 6 (2014) 14354–14359.
[36] F. Saleki, A. Mohammadi, S.E. Moosavifard, A. Hafizi, M.R. Rahimpour, J. Colloid Interface Sci. 556 (2019) 83–91.
[37] D. Yu, B. Wu, L. Ge, et al., J. Mater. Chem. A 4 (2016) 10878–10884.
[38] Y. Guo, C. Wu, N.W. Li, S. Yuan, L. Yu, J. Mater. Chem. A 7 (2019) 25247–25253.
[39] B.Y. Guan, A. Kushima, L. Yu, et al., Adv. Mater. 29 (2017) 1605902.
[40] R. Kumar, P. Rai, A. Sharma, J. Mater. Chem. A 4 (2016) 9822–9831.
[41] B. Huang, W. Wang, T. Pu, et al., Chem. Eng. J. 375 (2019) 121969.
[42] H. Zheng, Q. Zhang, H. Gao, et al., Energy Storage Mater. 22 (2019) 128–137.
[43] F. Wu, C. Yu, W. Liu, et al., J. Mater. Chem. A 3 (2015) 16728–16736.